energies

MDPI

Article

Design and Analysis of a Series-Type Permanent Magnet Axial Flux-Switching Memory Machine

Nian Li *, Da Xu, Xiangjun Hao and Jianhui Li

School of Automation, Nanjing University of Science and Technology, Nanjing 210094, China
* Correspondence: nian.li@njust.edu.cn

Abstract: This paper presents a new topology of an axial flux-switching memory machine with series-type permanent magnets (SPMs) to improve the flux regulation capability. The key idea was to combine low coercive force (LCF) PMs, which can be magnetized and demagnetized readily, with high coercive force (HCF) PMs in series to provide a variable air-gap magnetic flux. The flux regulating principle and the forward magnetization effect of HCF PMs on LCF PMs are presented and discussed. Based on 3D finite element analysis (FEA), the magnetization variation of LCF PMs and the electromagnetic performances of the machine under different magnetization states were investigated. Simulation results showed that the air-gap magnetic flux could be weakened by up to 45% by using a magnetization current impulse, significantly extending the PM motor's flux-weakening speed range. Finally, a prototype machine was built, and experiments were performed to validate the predictions. The basic experimental validation shows that the measured back-EMF and the flux regulating characteristic matched the 3D FEA results well.

Keywords: design; analysis; axial flux; flux-switching; memory machine; series PM; magnetization; demagnetization

Citation: Li, N.; Xu, D.; Hao, X.; Li, J. Design and Analysis of a Series-Type Permanent Magnet Axial Flux-Switching Memory Machine. *Energies* **2022**, *15*, 8954. https://doi.org/10.3390/en15238954

Academic Editors: Hui Yang, Qian Chen and Yu Wang

Received: 3 November 2022
Accepted: 23 November 2022
Published: 26 November 2022

1. Introduction

Permanent magnet (PM) memory machines or variable PM flux machines are a class of permanent magnet machines that can achieve direct PM flux regulation by changing the magnetization state of the low coercive force (LCF) PMs, such as Alnico, through pulse currents [1]. Compared to traditional PM machines, PM memory machines do not require a continuous flux-weakening current, and thus, they have the potential to eliminate the copper loss caused by the d-axis flux-weakening current. Therefore, PM memory machines exhibit the merits of an extended speed range as well as improved efficiency in the speed range above the rated speed [1–4], making them particularly suitable for driving cycle applications such as traction applications.

The feasibility of using LCF PMs for flux weakening was first investigated by Vlado Ostovic in 2001 [5]. However, the original PM memory machines had some inherent problems. LCF PMs, e.g., Alnico, are susceptible to the armature field due to their relatively low coercivities, and it is difficult to provide a high magnetic flux comparable with high coercive force (HCF) PMs using traditional magnetic designs [4,6,7]. Therefore, non-conventional magnetic circuit designs are required to achieve a high air-gap flux density in the PM memory machine [4,6]. This, however, could result in complex rotor and/or stator structures and possibly cause reliability issues.

To improve the air-gap flux density, an additional HCF PM can be introduced into the PM memory machine to assist the LCF PM, resulting in a hybrid PM memory machine [8–17]. There are two basic configurations for hybrid PMs: the parallel-type PM (PPM) and the series-type PM (SPM). By arranging the HCF and LCF PMs in parallel, the hybrid PM memory machine can produce a controllable high air-gap magnetic flux, which can not only yield a wide speed range but also maintain the high-power density of PM machines.

Although the PPM is the most common configuration that can offer a relatively high magnetic flux regulation capability, there exists a cross-coupling effect between the HCF and LCF PMs [8,9]. The magnetomotive force (MMF) of HCF PMs can lower the operating point of LCF PMs or, in the worst case, even demagnetize the LCF PMs due to their unbalanced MMFs, resulting in reduced flux regulation capability as well as air-gap flux density.

In the SPM memory machine, the HCF and LCF PMs are magnetically connected in series. While the HCF PM provides a constant MMF, the LCF PM provides a variable one, so the total MMF provided is variable [2,14–17]. This structure can eliminate the impact of the cross-coupling effect, such that unintentional demagnetization of the LCF PM due to the magnetic field produced by the armature current can be prevented, and the LCF PM can work more stably. However, most studies on memory machines with SPM configurations have been focused on radial field-type machines, with hardly any attention given to axial-type machines. In addition, most of the proposed SPM memory machines are rotor PM machines, in which armature winding is also used for changing the magnetization state of the LCF PMs. The amplitude of the magnetization control current, typically several times that of the rated current, poses a big challenge for armature winding and may result in an oversized machine inverter [18,19]. Furthermore, the use of d-axis current for magnetization variation requires knowledge of the rotor position and complicates the vector control of the machine. An alternative solution is incorporating additional DC magnetizing winding to produce the magnetizing current for direct PM magnetization control, hence avoiding the complicated current control and oversized machine inverter [20]. Additional DC winding also enables further flux weakening or flux enhancement when used as hybrid winding [21]. Inevitably, this will somewhat increase the overall size of the machine and slightly complicate the machine system.

This paper presents a novel series-type PM axial flux-switching memory (SPM-AFSM) machine with additional excitation winding PMs on the stator. The flux regulating principle and the forward magnetization effect due to HCF PMs are presented. The impact of the PM combination on flux regulation capability and the magnetization state control current is investigated. Finally, machine performance is evaluated by three-dimensional finite element analysis (3D-FEA). A prototype machine is manufactured and tested to validate the model and analysis.

2. Topology and Flux Control Principle

2.1. Machine Topology

Figure 1 shows the topology of the proposed double stator single rotor SPM-AFSM machine. The machine consists of two external stators and one inner rotor. A typical 12/10-pole combination, as in traditional flux-switching permanent magnet (FSPM) machines, was used [22]. The LCF and HCF PMs used for the proposed machine were Alnico 9 and NdFeB 35, respectively. NdFeB 35 was chosen because it can provide a relatively high coercive force at an economical price. Their magnetic properties are summarized in Table 1. Two types of PMs with identical magnetization directions were inserted into the stator in series. In order to change the magnetization of the LCF PM, independent magnetization winding was introduced to the inner sides of the stators. The excitation winding was fed by an independent capacitive-discharge magnetizer that will be presented in the experiment section.

Table 1. Magnetic properties of the PMs.

	Residual Flux Density Br (T)	**Coercive Force Hc (KA/m)**	**Operating Temperature °C**
Alnico 9	1.05	119	20
NdFeB 35	1.2	889	20

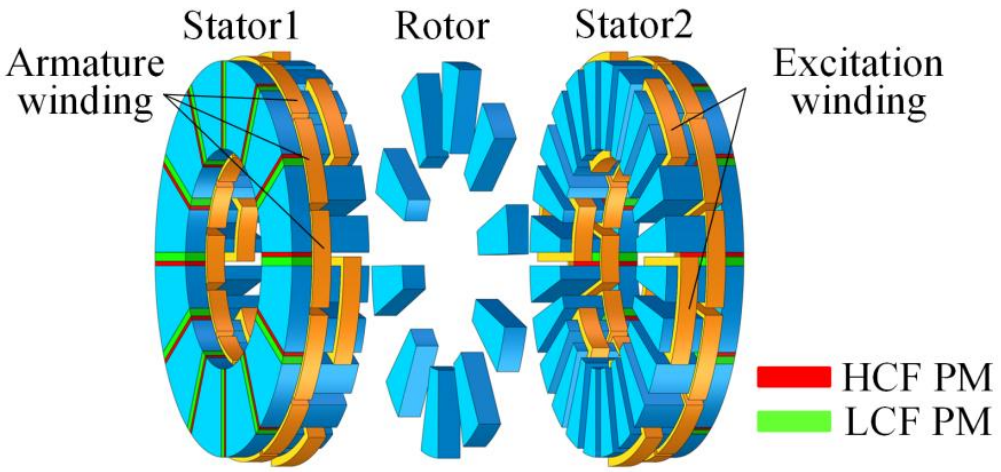

Figure 1. Machine configuration.

2.2. Description of the Flux Control Principle Based on the Hysteresis Model

Figure 2 shows the flux paths in the SPM-AFSM machine during the magnetization regulating process. The main magnetic fluxes produced by the SPM and the excitation winding are respectively represented by the solid and dashed lines. The magnetizing process presented in Figure 2a shows the case in which the current in the excitation winding produces an MMF, aiding that of the SPM. In contrast, supplying a current in the opposite direction into the excitation winding, as shown in Figure 2b, will demagnetize the LCF PM.

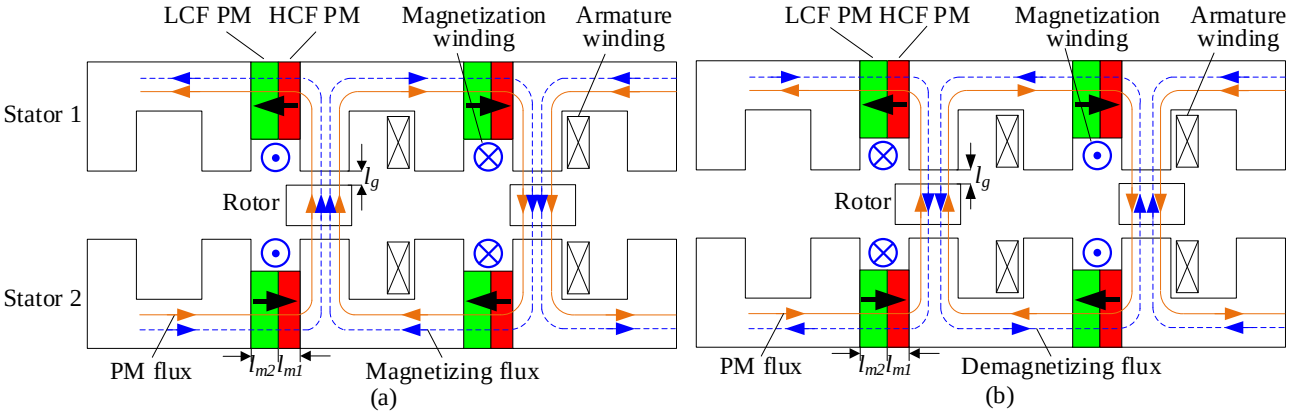

Figure 2. Magnetic flux paths during magnetization: (**a**) magnetizing process; (**b**) demagnetizing process.

Given the main magnetic flux paths in Figure 2, the following can be obtained by applying Ampere's law along the main magnetic flux paths:

$$2H_{m1}l_{m1} + 2H_{m2}l_{m2} + \int_N^S \vec{H_l} * \vec{dl} = 2N_f I_f \tag{1}$$

where H_{m1} and H_{m2} are the average fields over the length of the path in the PMs, H_l is the magnetic field along the flux line outside the PMs, l_{m1} and l_{m2} are the thicknesses of the PMs, N and S are the ends of the SPM with polarities of N and S, N_f is the number of turns of the excitation winding, and I_f is the magnetizing or demagnetizing current.

Whether the current in the excitation winding produces an MMF that magnetizes or demagnetizes the LCF PM depends on the current direction. By integrating the field strength along the magnetic flux paths, Equation (1) becomes:

$$\frac{\phi_m}{2P_t} = N_f I_f - H_{m1}l_{m1} - H_{m2}l_{m2} \tag{2}$$

where ϕ_m is the total flux produced by the SPM, and P_t is the permeance of the main magnetic flux, exclusive of the permeance of the path within the PMs. As long as the permeability of the steel is high relative to air, the permeance will be mainly determined by the air-gap permeance.

For the HCF PM, the magnetization was kept constant during the flux regulation, and the demagnetization curve can be expressed in the linear form as

$$B_{m1} = B_{r1} + \mu_0 \mu_{r1} H_{m1} \tag{3}$$

where B_{m1} is the average flux density within the HCF PM, μ_{r1} is the recoil permeability, and B_{r1} is the residual flux density.

In the discussion below, the leakage flux was neglected for simplicity. Thus, the magnetic flux produced is confined to the core and the same amount of magnetic flux passes the SPMs and the air gap, i.e.,

$$\phi_m = B_{m1} S_{m1} = B_{m2} S_{m2} \tag{4}$$

$$S_{m1} = S_{m2} \tag{5}$$

where S_{m1} and S_{m2} correspond to the cross-sectional area of HCF and LCF PMs, respectively. Solving Equations (2)–(5) for B_{m2}, a constant B_{m2}/H_{m2} relationship, i.e., the so-called load line, can be obtained as follows:

$$B_{m2} = k\left(\frac{N_f I_f}{l_{m2}} - H_{c1}\frac{l_{m1}}{l_{m2}} - H_{m2}\right) \tag{6}$$

where H_{c1} is the coercive force of the HCF PM and $k = l_{m2}/\left(\frac{S_{m2}}{2P_t} + \frac{l_{m1}}{\mu_0 \mu_{r1}}\right)$.

From (6), it can be inferred that in addition to the internal field H_{m2}, the magnetization current and MMF of the HCF PM can be considered as the external excitations to the LCF PM. The MMF of the HCF PM will move the load line of the LCF PM $H_{c1} l_{m1}/l_{m2}$ to the right along the horizontal axis.

As the magnetization and demagnetization of the LCF PM are characterized by hysteresis, the current operating point of the LCF PM depends on the history of magnetization [23]. The classic Preisach model, coupling the magnetic circuit, was used to model the hysteresis behavior of the LCF PM. The dependence of magnetization on the magnetic field is formulated as follows:

$$B_{m2} = P(H_{m2}) \tag{7}$$

where P stands for the Preisach model of the LCF PM.

By combining Equations (6) and (7), the operating point trajectory of the LCF PM during the magnetizing and demagnetizing processes can be obtained, as shown in Figure 3a,b, respectively. The operating points stabilized at different locations on the load line in different magnetization states. When the LCF PM was completely magnetized, the operating point was located at point A on the descending branch of the major loop. As the magnetization of the LCF PM decreased, the stabilized operating point moved down along the load line towards the first quadrant and finally settled at point B on the ascending branch of the major loop. Although the operating point can be further decreased by the demagnetizing current, it will return to point B after the current is switched off due to the forward magnetization of the HCF PM. This forward magnetization effect will magnetize the LCF PM, making it hard for it to be further demagnetized. Thus, the operating point of the LCF PM under different magnetizations will be constrained within points A and B.

Between points A and B, local minor loops were formed within the major loop due to the current pulses shown in Figure 3c. The operating point can only move to a new position when the amplitude of the applied pulse current exceeds the previous one. Otherwise, the LCF PM will maintain or "memorize" its magnetization state. Taking advantage of the LCF

PM's ability to change and "memorize" its magnetization state, one can readily adjust the magnetic flux produced by the SPM.

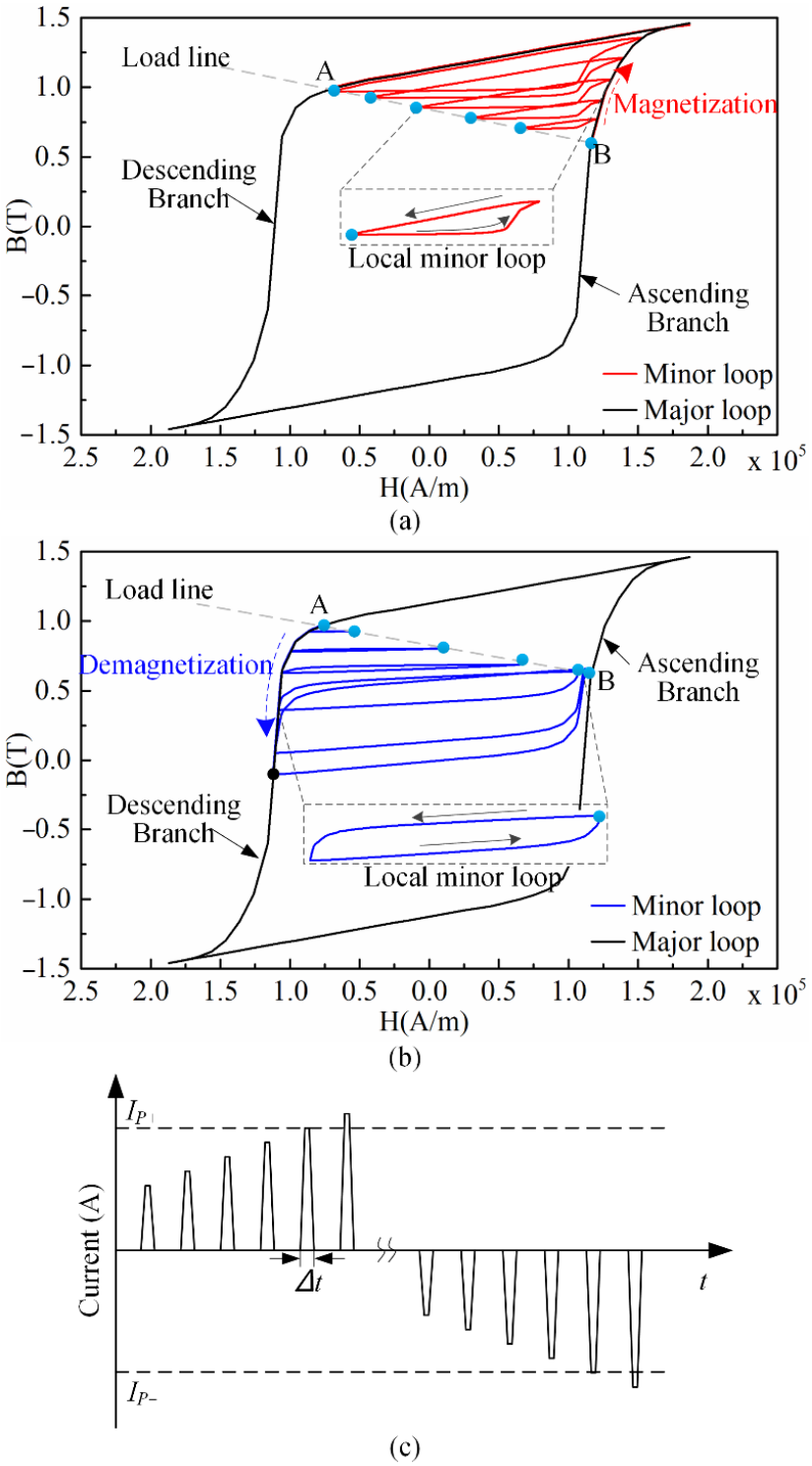

Figure 3. Magnetization and demagnetization processes under a monotonically changing field. (**a**) Magnetization. (**b**) Demagnetization. (**c**) Current pulses.

A current pulse exceeding I_{P+} is required to completely magnetize the LCF PM. Contrarily, a current pulse smaller than I_{P-} will demagnetize the LCF PM, moving its operating point to B. It should be noted that increasing the demagnetizing current will not

further decrease the operating point but will increase the risk of demagnetizing the HCF PM. Therefore, the amplitude of the demagnetizing current pulse should not exceed $I_{P\_}$.

3. Design of the SPM-AFSM Machine

The design of the SPM-AFSM machine is basically similar to that of conventional axial flux-switching PM machines. The difference is that modifications need to be made to the stator to incorporate the SPM and excitation winding for flux regulation. Since the SPM needs to provide adjustable magnetic flux under different operation conditions, special attention needs to be paid to its size design. Excitation winding should be able to provide a sufficiently large excitation field to fully magnetize and demagnetize LCF PMs according to the operating conditions. It should be noted that the design of the machine only considers electromagnetic aspects; the thermal and mechanical constraints are not considered. Figure 4 illustrates the structure of the initial design.

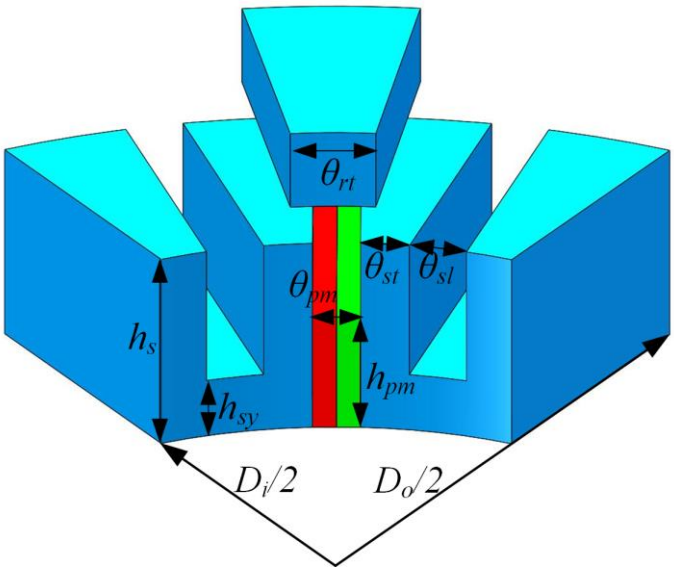

Figure 4. Original design structure of the machine with the rotor at the q-axis position.

3.1. Dimensioning Key Parameters

The SPM-AFSM machine was designed with the LCF PMs fully magnetized. The outer diameter of the proposed machine is given by the sizing equation derived from the output power equation [24]. The sizing equation can be expressed as

$$D_o = \sqrt[3]{\frac{\epsilon P_O}{\pi^3 \frac{p_r}{p_s} \alpha_s k_D k_w n A B_m \eta cos\phi}} \tag{8}$$

where D_o is the outer diameter, P_O is the output power with LCF PMs being fully magnetized, ϵ is the phase back-EMF to phase voltage ratio, p_r is the rotor pole number, p_s is the stator pole number, α_s is the stator pole-arc coefficient, k_D is a factor related to the inner to outer diameter ratio k_d and is expressed as $k_D = \frac{1}{8}(1 + k_d)(1 - k_d^2)$, k_w is the winding factor, n is the rotating speed, A is the electrical load, B_m is the peak magnetic flux density that can be produced in the air-gap with the LCF PMs fully magnetized, η is the efficiency, and $cos\phi$ is the power factor.

After the outer diameter of the machine is determined according to Equation (8), the turns of the winding can be calculated by the initial stator tooth angle θ_{st}, and the stator slot angle θ_{sl} and PM angle θ_{pm} in the inner diameter, as shown in Figure 4, were set to 7.5 degrees. According to a previously designed and prototyped AFSM machine [24], the optimized rotor tooth angle is usually 1.6 times the stator tooth angle to obtain a sinusoidal back-EMF. The number of armature turns per phase can be roughly chosen on the basis of

the assumed magnetic flux density and the given phase back-EMF, assuming the total flux produced by the SPM flows into the stator tooth and the stator yoke when the rotor pole is aligned with the stator pole. The flux density of the stator yoke can be calculated by

$$B_r = \frac{2B_m S_{sp}}{h_{sy}(D_o - D_i)s_f} \tag{9}$$

where S_{sp} is the stator pole surface area, h_{sy} is the height of the stator yoke, and s_f is the stacking factor of the core lamination.

The slot area required to allocate the armature winding is obtained as the product of the slot width and slot height.

$$S_{sl} = \theta_{sl} D_i (h_s - h_{sy})/2 \tag{10}$$

The slot area can also be expressed as

$$S_{sl} = 2N_c A_{cu}/k_{cu} \tag{11}$$

where N_c is the number of conductors per coil, A_{cu} is the copper area, and k_{cu} is the filling factor. Thus, the slot height can be calculated.

The modifications in the rotor tooth and stator tooth angle will be described later based on SPM dimensions and the magnetization performance.

3.2. Design of the SPM

It can be inferred from Figure 3 that the load line affects the highest and lowest operating points of the LCF PM and the flux regulation capability of the proposed machine. Once the grade of PMs is selected and the structure of the main magnetic circuit is determined, the flux regulation capability will be mainly related to the dimensions of the SPM. The descending branch of the major loop, as shown in Figure 3, can be expressed as

$$B_{m2} = F(H_{m2}) \tag{12}$$

The nonlinearity between H_{m2} and B_{m2} is a single-valued function. By combining Equations (6) and (12), working point A can be solved numerically and the maximum magnet flux provided by the SPM can be estimated.

The ascending branch of the major loop can be derived from the descending branch due to the central symmetry of the major loop

$$B_{m2} = -F(-H_{m2}) \tag{13}$$

Similarly, working point B can be solved numerically by combining Equations (6) and (13). The minimum magnet flux provided by the SPM can be estimated.

A flux regulation factor in the proposed machine can be formulated as:

$$k_f = \frac{\Phi_{fmax} - \Phi_{fmin}}{\Phi_{fmax}} \tag{14}$$

where Φ_{fmax} is the maximum flux produced by the SPM with the LCF PMs fully magnetized, and Φ_{fmin} is the minimum flux produced by the SPM with the LCF PMs demagnetized. For the SPM, k_f is in the range of 0 to 1. From [24], the minimum flux that determines the peak speed can be calculated by voltage equations, neglecting the resistance voltage drop.

Figure 5 shows the effect of the thickness of the LCF PM on the k_f and the operating point of the LCF PM obtained by the analytical method and 3D-FEA. As shown, the flux regulation capability increased with the increase in LCF PM thickness, while the magnetic flux density of the LCF PM decreased. This was mainly due to the relatively smaller coercive force of the LCF PM compared to that of the HCF PM. Thus, there is a tradeoff

between the flux regulation capability and the magnetic flux density in SPM memory machines, where improving one factor will come at the expense of deteriorating the other. At a given LCF PM ratio, the magnetic flux density increases as the thickness of the SPM increases. In contrast, the flux regulation capacity remains almost constant even when the thickness of the SPM varies. Thus, the ratio of the LCF PM to the total thickness of the SPM is a key factor in the determination of the flux regulation capacity. However, a higher current is required to regulate the magnetization state of the LCF PM. In this paper, the LCF and HCF PMs were set to 4 and 2 mm, respectively, to gain a good balance between the flux regulation capability and the magnetic flux density.

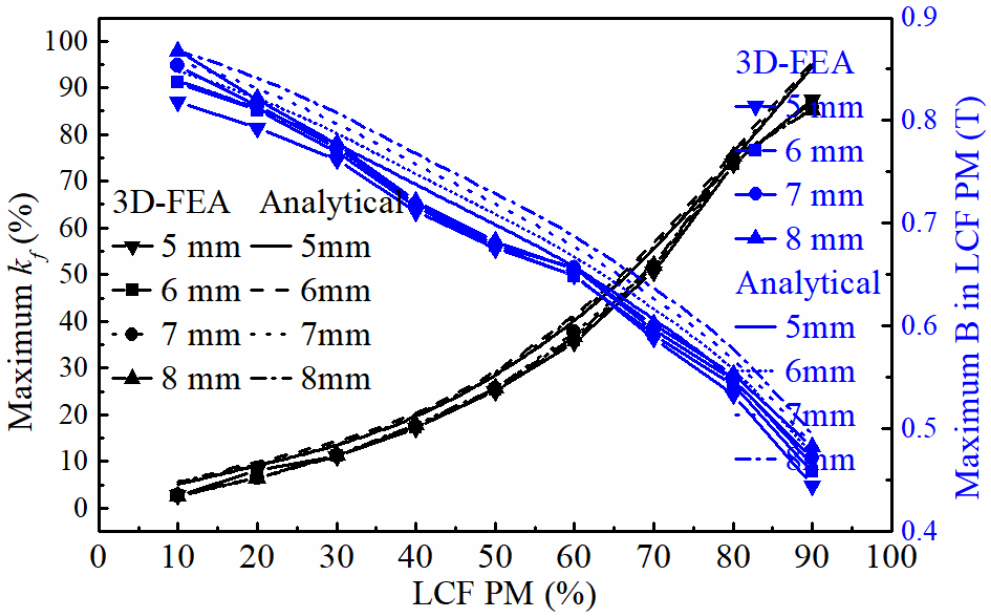

Figure 5. Maximum flux regulation capability and magnetic flux density inside the PMs as a function of the percentage of the LCF PM under varying thicknesses of the SPM.

3.3. Saturation Current Determination

In order to re-magnetize the LCF PMs to saturation, a magnetization field with sufficient amplitude is required. The corresponding current, which is determined by the magnetic flux distribution within the LCF PM during the magnetizing process, is denominated as the saturation current.

Figure 6 demonstrates the magnetic field distribution inside the LCF PMs at the time of magnetization under different magnetizing currents. As can be observed, the magnetic field near the outer radius reached saturation first, and the value gradually decreased along the direction towards the inner radius at different magnetizing currents. This was mainly due to the uneven permeability distribution of the machine. The resultant magnetic flux density inside the LCF PM versus the magnetization current is shown in Figure 7. The values are averages over five sample points on the surface of the LCF PM. As can be seen, the magnetic flux density increased as the magnetization current increased. At 120 A, the main part of the LCF PM was uniformly magnetized except for the fringe parts. The average resultant magnetic flux density at 120 A was almost equal to that of 160 A. Increasing the current will not significantly improve the resultant flux distribution but will pose a big challenge to both the machine and the magnetization circuit. Thus, 120 A was chosen as the saturation current able to provide a sufficient magnetization field.

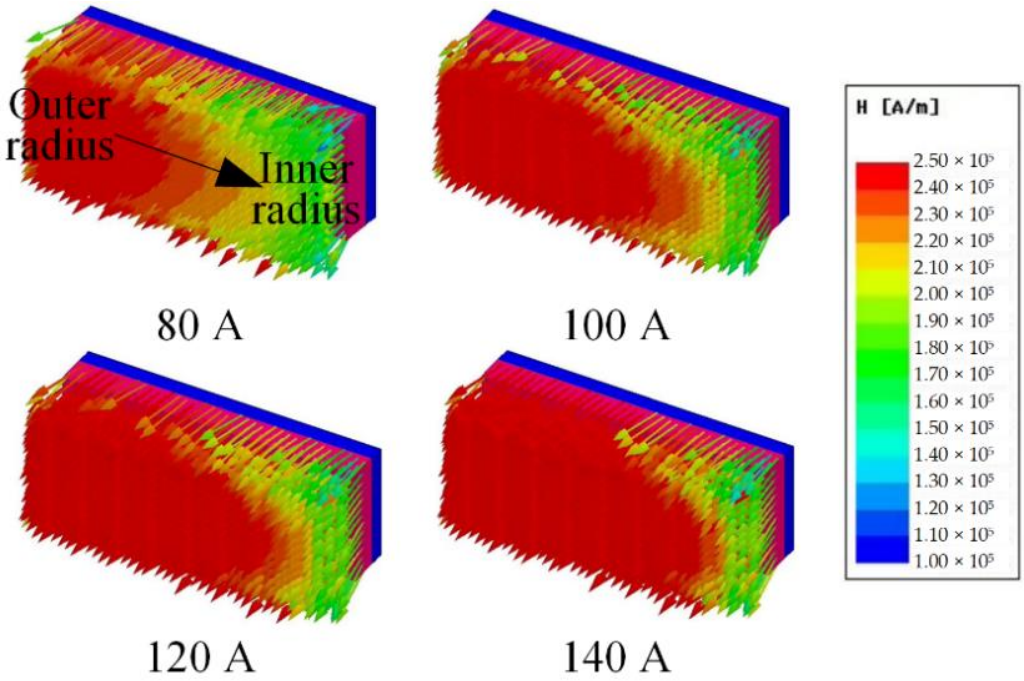

Figure 6. The field distribution inside the SPM under different magnetizing currents.

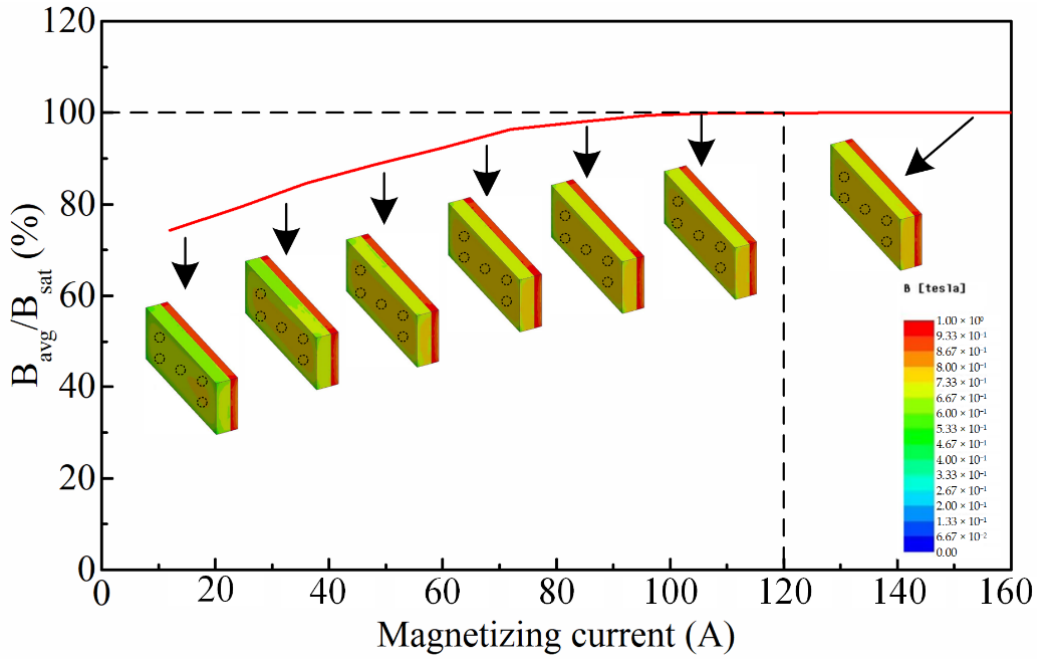

Figure 7. Average resultant magnetic flux density (normalized) on the sample points of the LCF PM after different magnetizing currents.

By fixing the total thickness of the SPM and the LCF PM ratio, the saturation current under different stator and rotor tooth angles was calculated, as shown in Figure 8. The stator tooth angle had a greater impact on the saturation current than the rotor tooth angle. The minimum saturation current was about 80 A when the stator tooth angle and the rotor tooth angle were 1 and 2.5 times that of the SPM, respectively. The rotor tooth angle was finally set to 1.8 times that of the SPM to achieve a sinusoidal back-EMF waveform. As a result, the minimum saturation current was slightly increased to about 100 A.

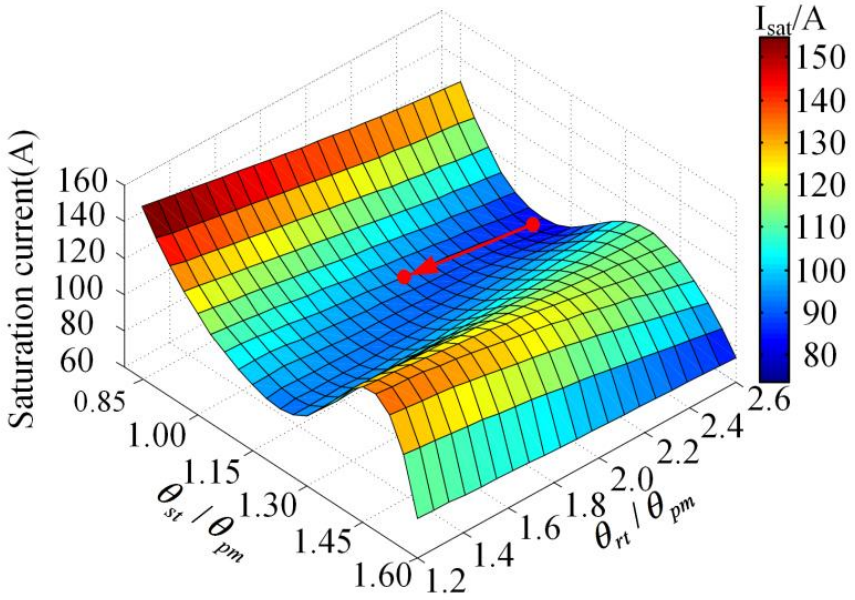

Figure 8. Saturation current versus stator and rotor tooth width.

The main design specifications and parameters of the machine are listed in Table 2.

Table 2. Main design specifications and parameters of the prototype.

Parameter	Value
Stator pole number	12
Rotor pole number	10
Stator outer diameter	160 mm
Stator inner diameter	97 mm
Axial length	84 mm
Air-gap length	2 mm
LCF magnet thickness	4 mm
HCF magnet thickness	2 mm
Magnet length	15 mm
Turns of excitation coil	60
Output power	250 W
Rated voltage	32 V
Rated speed	750 rpm
Rated frequency	125 Hz
Rated phase current	4 A

4. Electromagnetic Performance Analysis

In this section, the electromagnetic performance of the proposed SPM-AFSM machine under different magnetization states is evaluated using 3D-FEA.

4.1. Air-Gap Flux Density and EMF

The LCF PM was initially fully magnetized in the magnetization direction of the HCF PM. A demagnetizing current was then imposed to verify the flux controllability. Figure 9 shows the flux density distribution of the stator core and the SPM under maximum and minimum magnetization states. It can be observed that flux density can be effectively decreased by imposing a demagnetization current. Figure 10 shows the corresponding air-gap flux density distribution at the average radius. A maximum 0.7 T air-gap flux density was obtained with the LCF PM fully magnetized. In addition, the induced open circuit phase back-EMFs in different magnetization states are shown in Figure 11, which indicates a satisfactorily wide flux regulation capability.

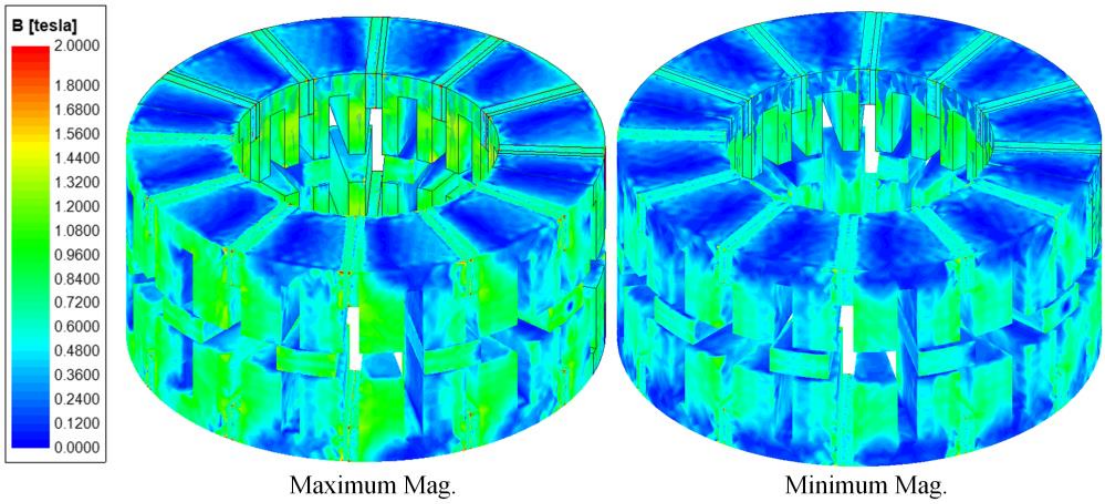

Figure 9. Flux density distribution under two typical magnetization states.

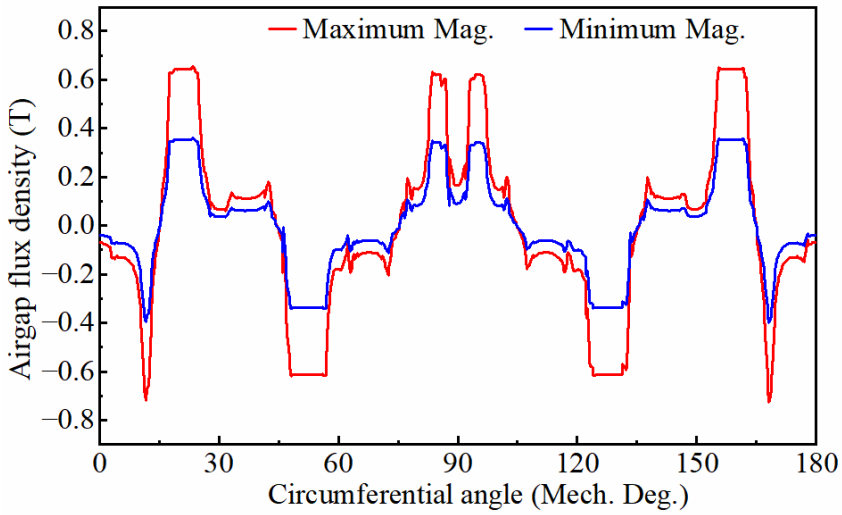

Figure 10. Air-gap flux density distribution at the average radius in the maximum and minimum magnetization states.

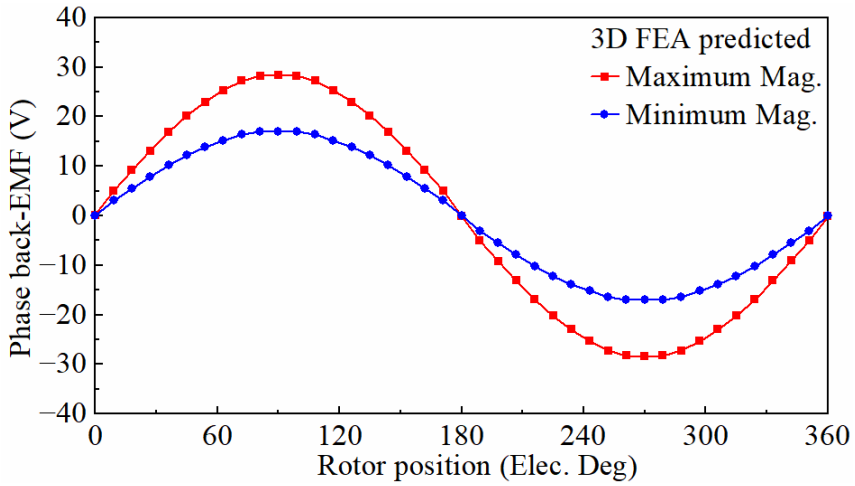

Figure 11. Open circuit phase back-EMFs under maximum and minimum magnetization states.

4.2. Torque

Figure 12 shows the cogging torque under two different magnetization states. The peak value of cogging torque decreased as the magnetization state decreased.

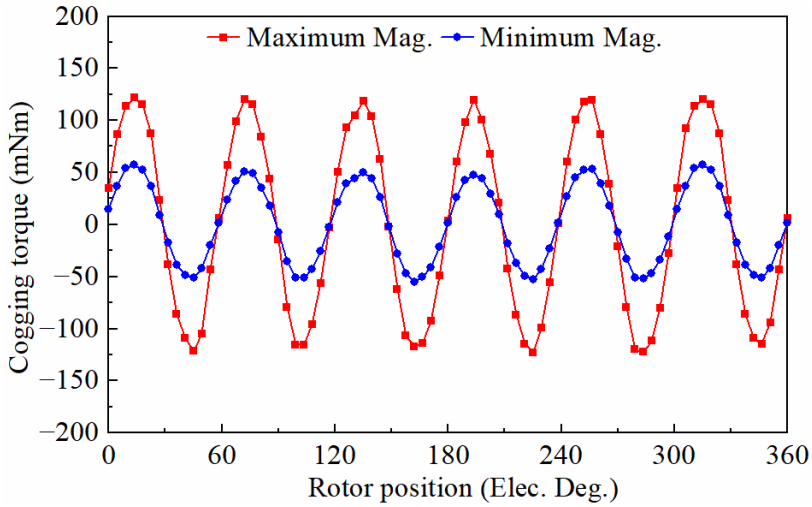

Figure 12. Torque waveforms in the maximum and minimum magnetization states.

Figure 13 shows the average torque at the rated current due to the magnetization state variation as a function of the current angle. There was a slight electrical angle shift of the maxima, indicating that the reluctance torque made a very small contribution to the electromagnetic torque. This coincides with the traditional AFSPM machines. Therefore, Id = 0 control was utilized in different magnetization states. Figure 14 compares the electromagnetic torque waveform at the rated current at the maximum and minimum magnetization states. We found that the average torque and torque ripple decreased with a decrease in the magnetization state. Moreover, a q-axis current (Iq) up to two times the rated current was applied at different initial magnetization states. By measuring the phase back-EMF after removing the load current Iq, the load effect was obtained and is shown in Figure 15. The results showed that back-EMF remained almost constant when the load current Iq was less than the rated current. This indicates that LCF PMs can maintain their magnetization even at lower magnetization levels under a load current less than the rated current. However, it should be mentioned that the back-EMF will vary slightly after a higher load current.

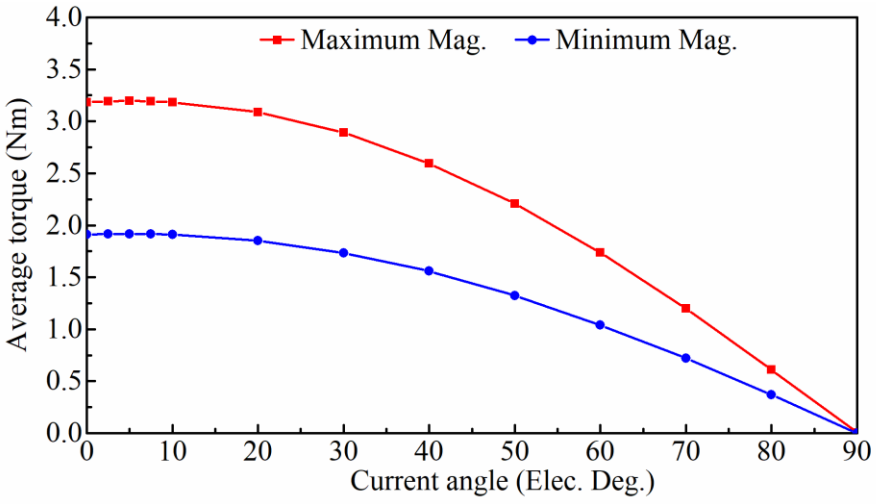

Figure 13. Average torque versus current angle in the maximum and minimum magnetization states.

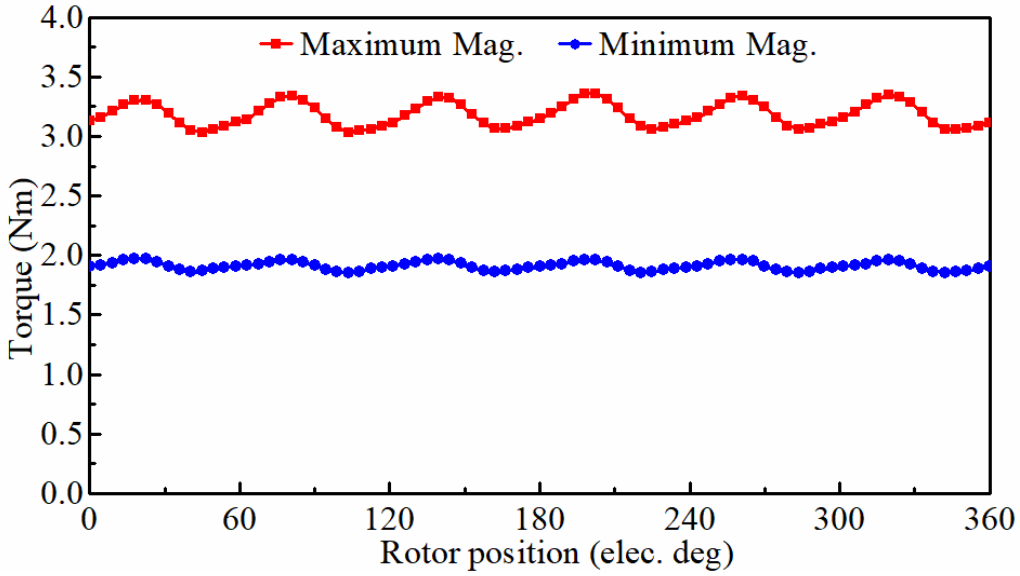

Figure 14. Electromagnetic torque waveforms at the rated current in the maximum and minimum magnetization states.

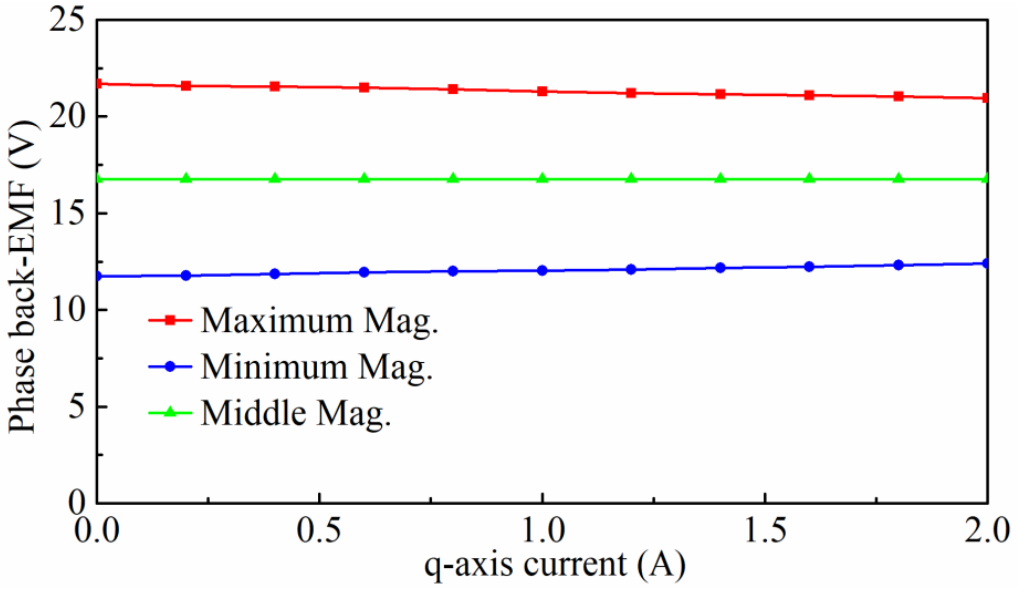

Figure 15. Back-EMFs after different load currents.

4.3. Flux Regulating Characteristic and Torque-Speed Curves

By plotting the back-EMF (RMS) against the magnetization control current, the back-EMF hysteresis loops from different initial magnetization states were obtained and are shown in Figure 16. The resultant back-EMF also presented the hysteretic property because of the inherent hysteretic property of the LCF PM. Thus, the back-EMF depends not only on the current imposed pulse current but also on the history of the imposed current. Notably, the whole hysteresis loop moved upward due to the forward magnetization of the adjacent HCF PM. The major loops show that the back-EMF approaches its maximum value at about 90 A. A further increase in the magnetizing current will not evidently increase the back-EMF. The minimum value was observed when the demagnetizing current reached about −80 A. The demagnetizing current should not be further decreased; otherwise, it will increase the risk of demagnetizing the HCF PM. As can be seen from Figure 16, the back-EMF decreased by up to 45% due to the magnetization variation.

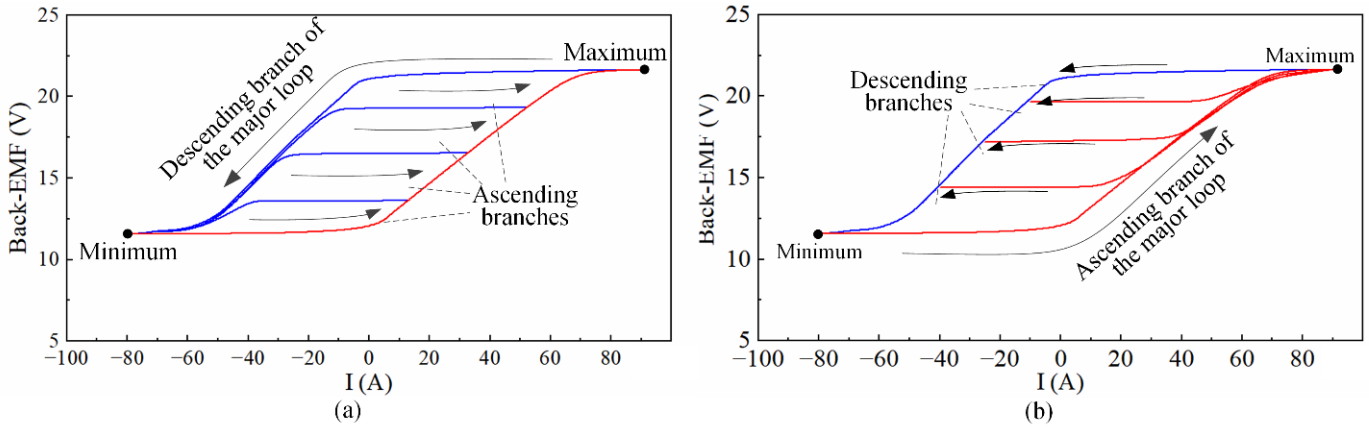

Figure 16. Back-EMF hysteresis loops of the proposed machine: (**a**) Magnetizing process; (**b**) Demagnetizing process.

The torque-speed curves and efficiency maps of the proposed machine under different magnetization states were calculated and are shown in Figure 17 to verify the advantages of the adjustable PM flux. The proposed machine can be treated as a traditional axial flux-switching PM machine when the LCF PMs are fully magnetized. By controlling the magnetization of the LCF PM to realize flux weakening, the proposed SPM-AFSPM machine is able to operate over a wide speed range without the use of –Id current. Thus, the copper loss of the machine in the high-speed region can be significantly reduced; 70% efficiency contours for the machine under different magnetization states were also presented. As can be seen, the 70% efficiency contour did not overlap at different magnetization states and moved towards the high-speed region for lower magnetization states. Improved efficiency can be achieved in the high-speed region by selecting the most appropriate magnetization state for different operating conditions.

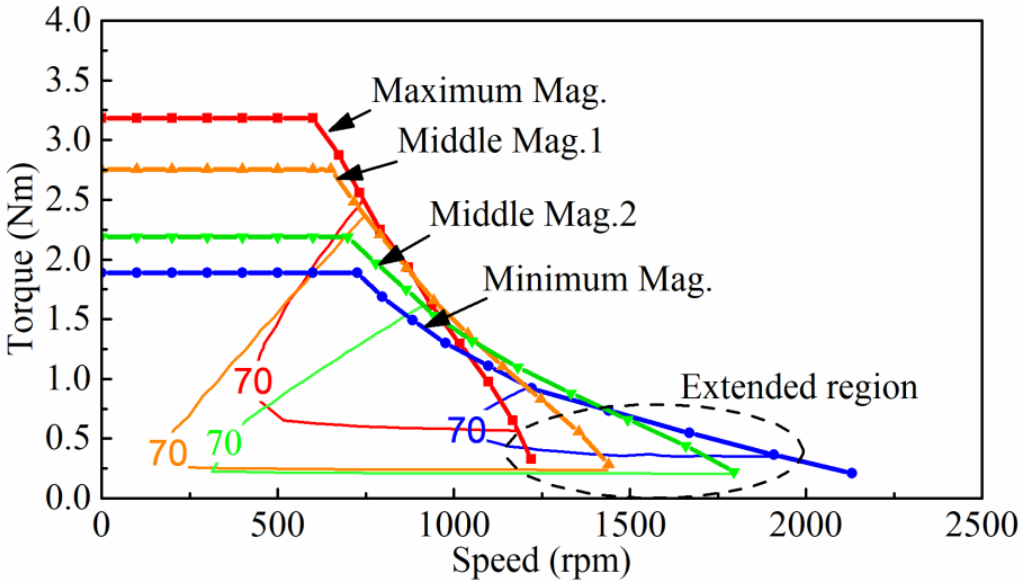

Figure 17. Torque-speed curves in four different magnetization states.

5. Experimental Validation

A prototype of the proposed machine was manufactured for experimental validation. Figure 18 shows the stator and rotor of the prototype and the experimental setup for testing the machine. An uncontrollable bidirectional capacitive-discharge magnetizer, as shown in Figure 18c, was used to magnetize and demagnetize the LCF PMs. Figure 18d

shows the schematic of the magnetizer. As can be seen, the magnetizer was composed of a three-phase diode bridge rectifier, a capacitor bank, an H-bridge for changing the pulse current direction, and a discharge branch consisting of a resistor and a circuit breaker. The large capacitor bank was charged by an adjustable three-phase power supply. When it was charged to the required voltage, the H-bridge was turned on to apply a magnetizing or demagnetizing current to the excitation winding. The relationship between the capacitor voltage and the induced peak pulse current was experimentally obtained in advance to facilitate the application of the required voltage and pulse current that can coerce the LCF PMs into the desired magnetization states. Although precise control of the pulse current by the presented uncontrollable bidirectional capacitive-discharge magnetizer was difficult due to the variation of the circuit parameters, its accuracy was sufficient for testing the magnetization and demagnetization performance of the prototype machine.

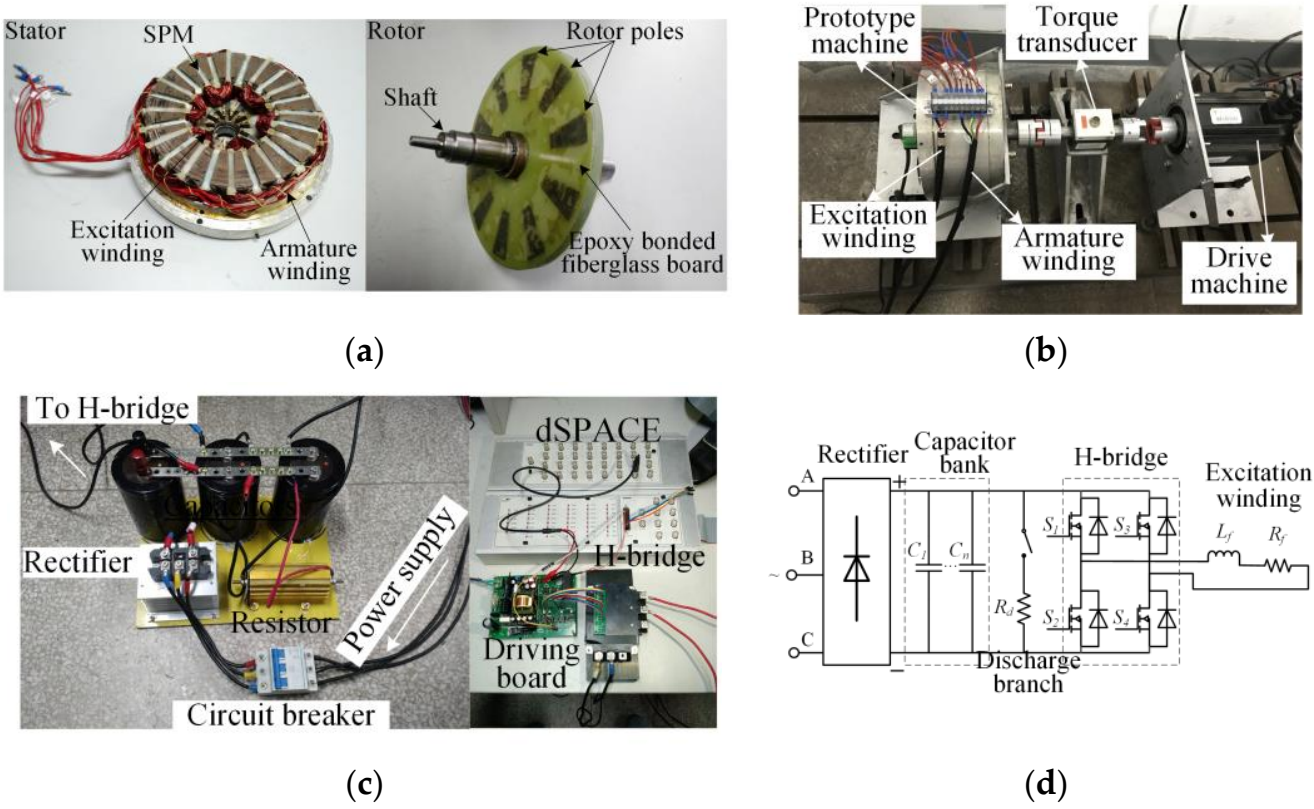

Figure 18. SPM-AFSM machine prototype and the experimental setup: (**a**) stator and rotor; (**b**) experimental setup; (**c**) bidirectional capacitive-discharger magnetizer; (**d**) schematic of the magnetizer.

The measured and 3D-FEA-predicted open circuit back-EMF and average torque of the prototype under two different magnetization states are shown in Figures 19 and 20, respectively. The measured back-EMF was slightly lower than the 3D-FEA-predicted one in the full magnetization state, which could be attributed to the insufficient magnetization of the fringe parts of the LCF PMs. The machine exhibited highly sinusoidal back-EMF waveforms in different magnetization states, which makes it suitable for brushless AC operation. The same is true for the average torque in different magnetization states. Overall, the experimental results agreed well with the predicted results of 3D-FEA.

To evaluate flux regulation effectiveness, the transient response of the back-EMF under a short duration of current pulses at the rated speed was measured and is shown in Figure 21. The measurement was performed when the LCF PMs were initially in the maximum or minimum magnetization state. During the flux regulation process, a current pulse of 0.1 s duration was imposed. As can be seen, the phase back-EMFs finally settled to about 17.5 V after the 40 A magnetizing current pulse died out. Similarly, it decreased from

21 V to about 15 V after the 40 A demagnetizing pulse current. The measured transient response of the back-EMFs demonstrates that PM flux linkage can be effectively controlled by a current pulse during operation. Since the excitation winding is only energized for tens of milliseconds, excitation losses associated with the magnetization control can be neglected.

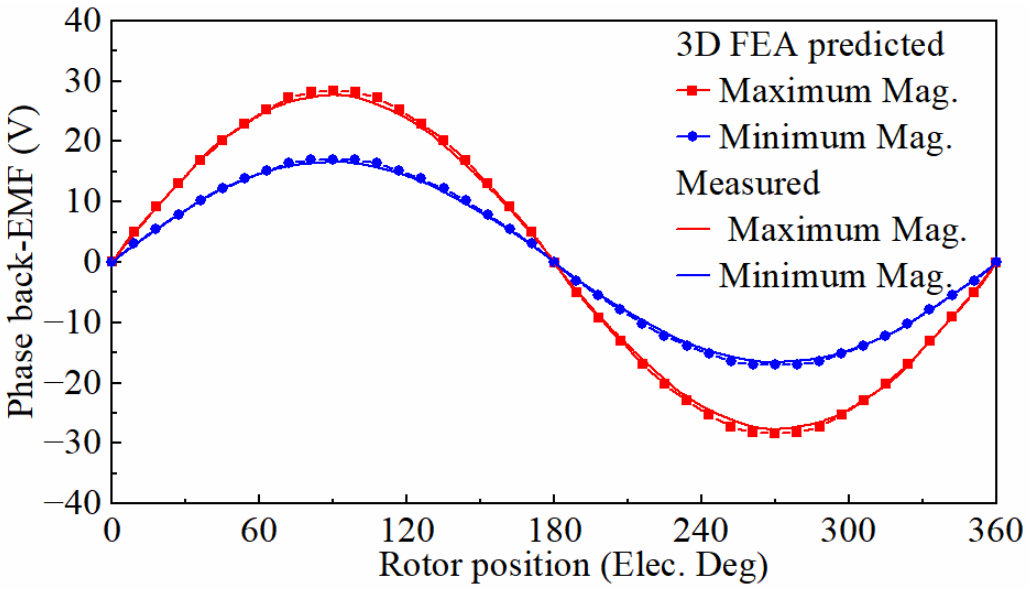

Figure 19. No load back-EMF in the maximum and minimum magnetization states.

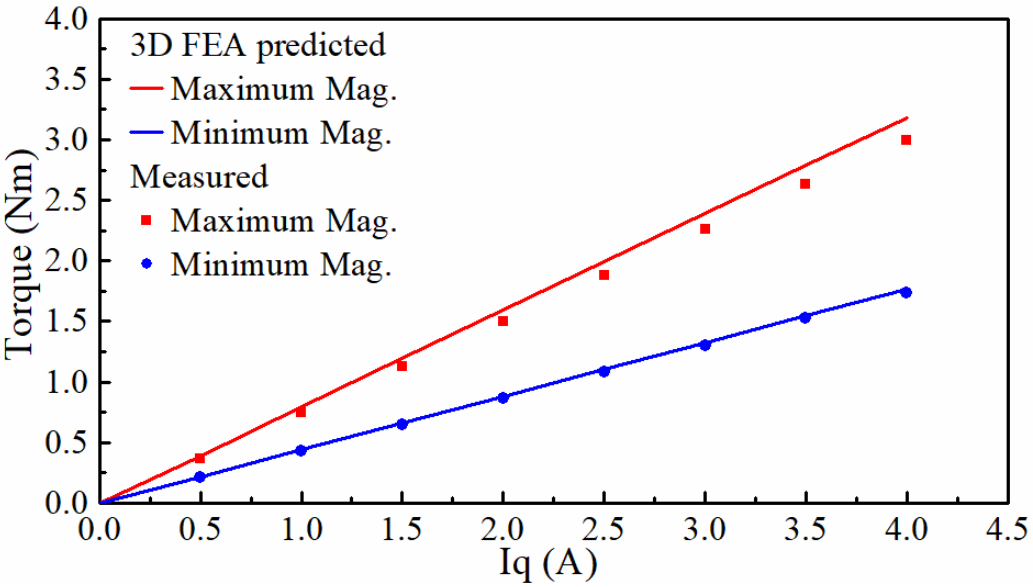

Figure 20. Average torque versus q-axis current in the maximum and minimum magnetization states.

Finally, by continuously performing magnetization or demagnetization from different initial magnetization states, the resultant back-EMFs in different magnetization states were measured and are shown in Figure 22. The measured maximum flux regulation capacity was approximately 40%, which is 5% smaller than the predicted value. The results demonstrate that the hysteresis loops can be used to characterize the change of back-EMFs due to pulse currents and provide information about flux regulation due to the magnetization variation in SPM memory machines.

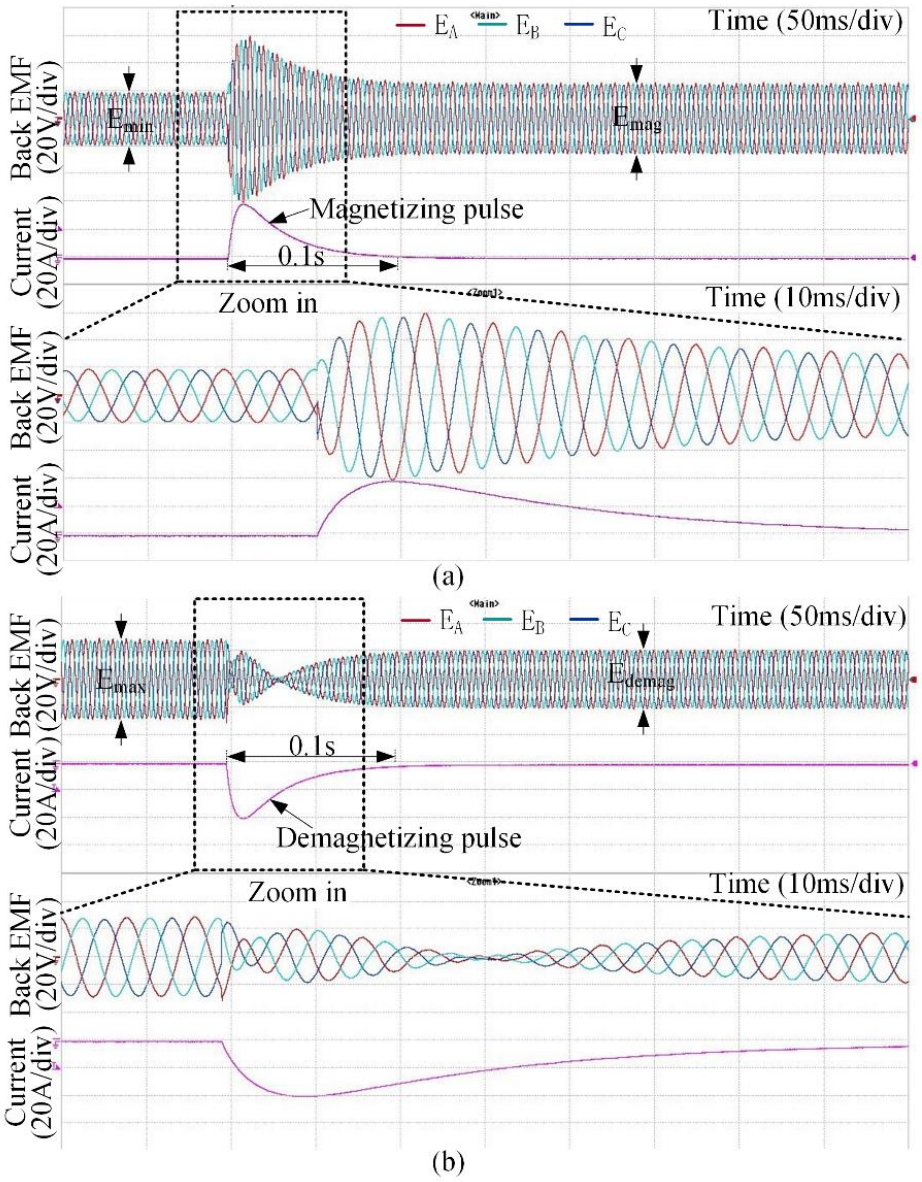

Figure 21. Measured transient response of back-EMFs under a short duration of current impulse at the rated speed: (**a**) magnetizing process; (**b**) demagnetizing process.

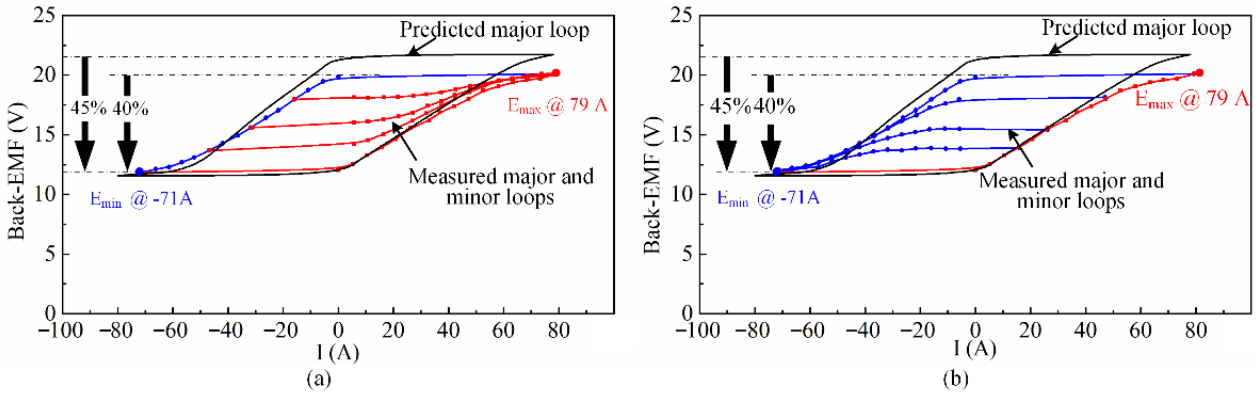

Figure 22. Resultant back-EMF hysteresis loop after magnetizing and demagnetizing from different initial magnetization states. (**a**) Magnetizing process; (**b**) demagnetizing process.

6. Conclusions

This paper has demonstrated the design and analysis of an axial flux-switching memory machine with an SPM for flux regulation. The work can be summarized as follows:

1. The ratio of the LCF PM is a key factor in determining the flux regulation capability. A higher LCF PM ratio is preferable for a wider flux regulation range. However, the air-gap flux density will be compromised if the total amount of PMs remains unchanged.
2. By varying the magnetization state of the LCF PM, the total magnetic flux produced by the SPM can be regulated. However, due to the forward magnetization of the HCF PM, the LCF PM can only change its magnetization state in the same magnetization direction as the adjacent HCF PM.
3. Both the simulated and experimentally measured back-EMFs showed the hysteresis characteristic due to the inherent hysteretic property of LCF PMs.
4. The magnetic flux can be controlled dynamically using current pulses at a small energy expense to achieve high efficiency in the high-speed region.

Although the proposed machine can offer the advantages mentioned in Section 4, the additional excitation winding and the separate drive for magnetization control add new challenges to the machine design. Future works should focus on the size reduction of the additional magnetization winding and magnetization circuits, alternative magnet combinations, and the selection of appropriate magnetization states for different machine operating conditions.

Author Contributions: Conceptualization, writing—review and editing N.L.; data curation, visualization, X.H. and J.L.; project administration, funding acquisition, D.X. All authors have read and agreed to the published version of the manuscript.

Funding: This research was funded by the National Natural Science Foundation of China, grant number 51807093,and the Jiangsu Provincial Key Laboratory of Smart Grid Technology and Equipment.

Data Availability Statement: Not applicable.

Conflicts of Interest: The authors declare no conflict of interest.

References

1. Athavale, A.; Reigosa, D.; Akatsu, K.; Sakai, K.; Lorenz, R.D. Scalability and Key Tradeoffs of Variable Flux PM Machines for EV Traction Motor Systems. In Proceedings of the 2018 IEEE Energy Conversion Congress and Exposition (ECCE), Portland, OR, USA, 23–27 September 2018; pp. 2292–2299.
2. Sakai, K.; Misu, D.; Yuki, K.; Yasui, K.; Hashiba, Y.; Takahashi, N. New generation motor for energy saving. In Proceedings of the 2010 International Power Electronics Conference-ECCE ASIA, Sapporo, Japan, 21–24 June 2010; pp. 1354–1358.
3. Han, M.; Besson, C.; Savary, A.; Becher, Y. Performance Assessment of a Variable-Flux Permanent-Magnet Memory Motor. *Int. J. Electr. Comput. Eng.* **2019**, *13*, 296–303.
4. Ibrahim, M.; Pillay, P. Design of high torque density variable flux permanent magnet machine using Alnico magnets. In Proceedings of the 2014 IEEE Energy Conversion Congress and Exposition (ECCE), Pittsburgh, PA, USA, 14–18 September 2014; pp. 3535–3540.
5. Ostovic, V. Memory motors-a new class of controllable flux PM machines for a true wide speed operation. In Proceedings of the Conference Record of the 2001 IEEE Industry Applications Conference 36th IAS Annual Meeting, Chicago, IL, USA, 30 September–4 October 2001; Volume 4, pp. 2577–2584.
6. Yang, H.; Liu, W.; Zheng, H.; Lin, H.; Zhu, Z.Q.; Peng, F.; Li, Y.; Lyu, S.; Huang, X.A. Novel Delta-Type Hybrid-Magnetic-Circuit Variable Flux Memory Machine for Electrified Vehicle Applications. *IEEE Trans. Transp. Electrif.* **2022**, *8*, 3512–3523. [CrossRef]
7. Yu, C.; Chau, K.T.; Liu, X.; Jiang, J.Z. A flux-mnemonic permanent magnet brushless motor for electric vehicles. *J. Appl. Phys.* **2008**, *103*, 07F103. [CrossRef]
8. Wu, D.; Zhu, Z.Q.; Liu, X.; Pride, A.; Deodhar, R.; Sasaki, T. Cross coupling effect in hybrid magnet memory motor. In Proceedings of the 7th IET International Conference on Power Electronics, Machines and Drives (PEMD 2014), Manchester, UK, 8–10 April 2014; pp. 1–6.
9. Li, Y.; Yang, H.; Lin, H. A Novel Stator Flux-Concentrated Hybrid Permanent Magnet Memory Machine. *IEEE Trans. Magn.* **2021**, *57*, 1–6. [CrossRef]
10. Zhu, X.; Quan, L.; Chen, D.; Cheng, M.; Hua, W.; Sun, X. Electromagnetic Performance Analysis of a New Stator-Permanent-Magnet Doubly Salient Flux Memory Motor Using a Piecewise-Linear Hysteresis Model. *IEEE Trans. Magn.* **2011**, *47*, 1106–1109. [CrossRef]

11. Yang, H.; Zheng, H.; Lin, H.; Zhu, Z.-Q.; Fu, W.; Liu, W.; Lei, J.; Lyu, S. Investigation of Hybrid-Magnet-Circuit Variable Flux Memory Machines with Different Hybrid Magnet Configurations. *IEEE Trans. Ind. Appl.* **2021**, *57*, 340–351. [CrossRef]
12. Liu, W.; Yang, H.; Lin, H. A Hybrid Field Analytical Method of Hybrid-Magnetic-Circuit Variable Flux Memory Machine Considering Magnet Hysteresis Nonlinearity. *IEEE Trans. Transp. Electrif.* **2021**, *7*, 2763–2774. [CrossRef]
13. Zhu, X.; Chen, Y.; Xiang, Z.; Yang, L.; Xu, L. Electromagnetic Performance Analysis of a New Stator-Partitioned Flux Memory Machine Capable of Online Flux Control. *IEEE Trans. Magn.* **2016**, *52*, 1–4. [CrossRef]
14. Maekawa, S.; Yuki, K.; Matsushita, M.; Nitta, I.; Hasegawa, Y.; Shiga, T.; Hosoito, T.; Nagai, K.; Kubota, H. Study of the Magnetization Method Suitable for Fractional-Slot Concentrated-Winding Variable Magnetomotive-Force Memory Motor. *IEEE Trans. Power Electron.* **2014**, *29*, 4877–4887. [CrossRef]
15. Wang, Y.; Niu, S.; Fu, W. Electromagnetic Performance Analysis of Novel Flux-Regulatable Permanent Magnet Machines for Wide Constant-Power Speed Range Operation. *Energies* **2015**, *8*, 13971–13984. [CrossRef]
16. Kim, J.-M.; Choi, J.-Y.; Lee, S.-H.; Jang, S.-M. Characteristic Analysis and Experiment of Surface-Mounted Type Variable-Flux Machines Considering Magnetization/Demagnetization Based on Electromagnetic Transfer Relations. *IEEE Trans. Magn.* **2014**, *50*, 1–4. [CrossRef]
17. Hua, H.; Zhu, Z.; Pride, A.; Deodhar, R.; Sasaki, T. A Novel Variable Flux Memory Machine with Series Hybrid Magnets. In Proceedings of the 2016 IEEE Energy Conversion Congress and Exposition (ECCE), Milwaukee, WI, USA, 18–22 September 2016.
18. Limsuwan, N.; Kato, T.; Akatsu, K.; Lorenz, R.D. Design and evaluation of a variable-flux flux-intensifying interior permanent magnet machine. *IEEE Trans. Ind. Appl.* **2012**, *50*, 3670–3677.
19. Tsunata, R.; Takemoto, M.; Ogasawara, S.; Orikawa, K. Variable Flux Memory Motor Employing Double-Layer Delta-Type PM Arrangement and Large Flux Barrier for Traction Applications. *IEEE Trans. Ind. Appl.* **2021**, *57*, 3545–3561. [CrossRef]
20. Yang, H.; Zhu, Z.Q.; Lin, H.; Zhan, H.L.; Hua, H.; Zhuang, E.; Fang, S.; Huang, Y. Hybrid-Excited Switched-Flux Hybrid Magnet Memory Machines. *IEEE Trans. Magn.* **2016**, *52*, 1–15. [CrossRef]
21. Hao, L.; Lin, M.; Li, W.; Luo, H.; Fu, X.; Jin, P. Novel Dual-Rotor Axial Field Flux-Switching Permanent Magnet Machine. *IEEE Trans. Magn.* **2012**, *48*, 4232–4235. [CrossRef]
22. Mayergoyz, I.D. *Mathematical Models of Hysteresis and Their Applications*; Elsevier: Amsterdam, The Netherlands, 2003.
23. Zhang, W.; Liang, X.; Lin, M.; Hao, L.; Li, N. Design and Analysis of Novel Hybrid-Excited Axial Field Flux-Switching Permanent Magnet Machines. *IEEE Trans. Appl. Supercond.* **2016**, *26*, 1–5. [CrossRef]
24. Gagas, B.S.; Sasaki, K.; Athavale, A.; Kato, T.; Lorenz, R.D. Magnet Temperature Effects on the Useful Properties of Variable Flux PM Synchronous Machines and a Mitigating Method for Magnetization Changes. *IEEE Trans. Ind. Appl.* **2017**, *53*, 2189–2199. [CrossRef]